

# Self-generated and interaction-induced hydrodynamic coupling and kinetic control of swarming

Yao-Li Chuang and Maria R. D’Orsogna

*Dept. of Mathematics, California State University, Northridge, Northridge, CA 91330*

Tom Chou

*Depts. of Biomathematics & Mathematics, UCLA, CA 90095-1766*

Mathematical models developed to describe the trajectories of “swarming” particles that interact through decentralized forces have shed light on the mechanisms of collective dynamics and self-organization. Besides coupling through direct pairwise forces, individuals can also interact via the medium in which they swim. We derive from first principles a three-dimensional theory of particle swarming that explicitly includes particle-fluid coupling, distinguishing between swimmer-induced and interaction-induced flows. Dynamics occurring in “clear fluids,” in which swimmers have full knowledge of their surroundings are also compared with those occurring in “opaque fluids” in which only velocities relative to the local fluid velocity are controlled. We show that short-ranged particle-particle interactions can lead to much longer-ranged fluid-mediated hydrodynamic forces, effectively amplifying the range between which particles interact. This induced fluid flow, along with self-generated flows, can conspire to profoundly affect swarm morphology, kinetically stabilizing or destabilizing swarm configurations. Depending upon the interaction potential, the mechanism of force-free swimming (*e.g.*, pushers or pullers), and the degree of fluid opaqueness, we find a number of new collective patterns including flocks with prolate or oblate shapes, recirculating peloton-like structures, and jet-like fluid flows that entrain particles in mill-like structures. Our results reveal how fluid-mediated interactions influence the self-organization, mobility and stability of three-dimensional swarms and suggest how they might be used to kinetically control their collective behavior.

PACS numbers:

The collective behavior of self-propelled agents in natural and artificial systems has been extensively studied[1–20]. Many of the lessons learned from experimental and theoretical work conducted on organisms as diverse as bacteria, ants, locusts, and birds [21–33] have been successfully applied to engineered robotic systems to help frame decentralized control strategies through ad-hoc algorithms [34–41]. In most theoretical “swarming” models, particles are assumed to be self-driven by internal mechanisms that impart a characteristic speed. A pairwise short-ranged repulsion and a longer-ranged, decaying attraction are typically employed as the most realistic choices when modeling individuals with a propensity to aggregate [8, 10, 42]. The interplay between self-propulsion, particle interactions, initial conditions, and number of particles is key in determining the large scale patterns that dynamically arise. In two dimensions, rotating mills and translating flocks are often observed, the latter configuration also arising in three-dimensions [8, 9, 16, 18, 43, 44]. It is possible to classify swarm morphology in terms of interaction strength and length scales, as shown for particles coupled via conserved forces derived from the Morse potential [16, 18]. Moreover, externally applied potentials and noise can be used to trigger transitions between coherent and disordered structures [3, 43, 44].

Although different rules for the characteristic speed have been proposed [8, 9, 16], most studies so far have focused on self-propelled agents in “vacuum”, ignoring the medium in which nearly all real systems operate. One exception is the literature on swimmers wherein models have been developed for a single or a few organisms that propel themselves in viscous [45–53] and non-Newtonian fluids [53–61]. In particular, one can derive a set of “two-fluid” hydrodynamic equations, where fluid flow as well as swimmer density and motion are modeled as continuous fields [62]. As illustrated in the Supplementary Information (SI) however, these continuum models may not always display the rich features observed when particles retain their discreteness, especially in terms of swarm morphology, stability and self-organization. A more microscopic three-dimensional theory incorporating fluid interactions into “agent-based” kinetic theories would thus provide a more complete framework for efficiently studying the collective dynamics of self-propelled, hydrodynamically interacting particles. A possible starting point would be to assume that the fluid medium leads to direct coupling between particle velocities and build this effect into existing models using, for example, the Cucker-Smale velocity matching mechanism. Here, particle  $i$  is subject to an additional force due to the presence of particle  $j$ , given by  $\mathbf{v}_j - \mathbf{v}_i$  and modulated by a distance-dependent prefactor  $g(|\mathbf{r}_i - \mathbf{r}_j|)$  [63–65]. Because of this simple mathematical form, Cucker-Smale type interactions have been used extensively to study swarming, with coherent morphologies arising depending on the form of  $g(|\mathbf{r}_i - \mathbf{r}_j|)$ . Although not explicitly meant to model fluid-mediated couplings, a heuristic Cucker-Smale-type interaction could be constructed by choosing an appropriate form for  $g(|\mathbf{r}_i - \mathbf{r}_j|)$  or different powers of  $|\mathbf{v}_i - \mathbf{v}_j|$ . Whether such an approach would be consistent with more microscopic, first-principle derivations of fluid-mediated particle-particle interactions is however unclear.

The goal of this paper is to understand how fluid flows arise from swarms of self-propelled discrete particles immersed in viscous media and how these fluid flows consequently affect particle dynamics and swarm morphologies. In low-Reynolds number Newtonian fluids, depending on its “stroke,” a self-propelled swimmer may generate a  $1/r^n$  fluid flow disturbance [53, 66–69]. The motion of a force-free swimmer arises from force dipoles or more complex force distributions, leading to  $n \geq 2$ . Flows also arise from particle-particle interactions, such as the Morse potential. These pair-wise interactions are typically shorter ranged than the  $1/r^n$  flows imparted by particle swimming. However, as we shall see, interaction forces can be transmitted to the surrounding fluid and collectively generate a much longer-ranged flow field, effectively *extending* the range of direct particle interaction. In particular, we find that potential-induced fluid flows scale as  $1/r$  [70–75] and are longer ranged than the self-induced  $1/r^n$ ,  $n \geq 2$  ones.

We explicitly formulate and numerically investigate the new interaction-induced fluid coupling mechanism described above, which, along with the self-induced flow field, controls the dynamics and collective patterns of self-propelled particles. Moreover, we examine two different types of fluids: “clear” and “opaque.” In a clear fluid, particles can “see” fixed markers and have direct knowledge of their motion in reference to the rest frame. Their absolute velocities can be directly controlled by their internal self-propelling mechanism. Here, the surrounding fluid simply imparts an additional drag force. In the richer and more interesting case of an opaque fluid, particles only have near-field vision and their velocities can be governed only in relation to the surrounding flow. In both cases, we systematically derive the effective particle-particle coupling arising from viscous Stokes flows and investigate their effects on coherent three dimensional swarming structures. We find that hydrodynamic couplings may nontrivially affect the morphology of emerging patterns, giving rise to surprising new structures such as distorted flocks, pelotons, core-filled mills, and mills that perpetually disband and reform.

### Fluid-coupled equations of motion

The equations of motion for particle  $i$  with mass  $m$ , at position  $\mathbf{r}_i(t)$ , and with lab-frame velocity  $\mathbf{v}_i(t)$  are

$$\dot{\mathbf{r}}_i = \mathbf{v}_i, \quad m\dot{\mathbf{v}}_i = \mathbf{f}_M(\mathbf{v}_i, \mathbf{u}(\mathbf{r}_i)) - \gamma(\mathbf{v}_i - \mathbf{u}(\mathbf{r}_i)) + \mathbf{f}_i, \quad (1)$$

where

$$\mathbf{f}_i = -\nabla_i \sum_{j \neq i} \Phi(|\mathbf{r}_i - \mathbf{r}_j|) \quad (2)$$

is the particle-particle interaction force on particle  $i$ ,  $\nabla_i \equiv \partial/\partial\mathbf{r}_i$ ,  $\Phi(|\mathbf{r}_i - \mathbf{r}_j|)$  is the direct pairwise interaction potential, and  $\mathbf{u}(\mathbf{r}_i)$  is the fluid velocity generated at position  $\mathbf{r}_i$  by the motion of all other particles in the absence of particle  $i$ . The term  $\mathbf{f}_M(\mathbf{v}_i, \mathbf{u}(\mathbf{r}_i))$  represents the self-propelling motility force on particle  $i$ , which can depend both on  $\mathbf{v}_i$  and  $\mathbf{u}(\mathbf{r}_i)$ . The drag force  $-\gamma(\mathbf{v}_i - \mathbf{u}(\mathbf{r}_i))$  on particle  $i$  is proportional to its velocity relative to that of the fluid. Without loss of generality, we will assume spherical particles with a small radius  $a$  and drag coefficient  $\gamma = 6\pi\eta a$ . While any potential can be used, we focus on the commonly studied Morse-type potential [8], given by the superposition of repulsive and attractive components

$$\Phi(|\mathbf{r}_i - \mathbf{r}_j|) = C_r e^{-\frac{|\mathbf{r}_i - \mathbf{r}_j|}{\ell_r}} - C_a e^{-\frac{|\mathbf{r}_i - \mathbf{r}_j|}{\ell_a}}. \quad (3)$$

The coefficients  $C_a$  and  $C_r$  in Eq. 3 define the strengths of the attractive and repulsive potentials, respectively and  $\ell_a$  and  $\ell_r$  specify their effective lengths of interaction. Several forms are possible for the motility force  $\mathbf{f}_M(\mathbf{v}_i, \mathbf{u}(\mathbf{r}_i))$ , depending on how the environment is to be modeled. Ignoring couplings to the surrounding medium and drag forces,  $\mathbf{f}_M$  is usually chosen to have nontrivial zeros. A typical choice is given by [16, 18, 44]

$$\mathbf{f}_M(\mathbf{v}_i) = (\alpha - \beta |\mathbf{v}_i|^2) \mathbf{v}_i \quad (4)$$

where  $\alpha$  and  $\beta$  represent self acceleration and deceleration, respectively. Setting  $\mathbf{f}_M(\mathbf{v}_i, \mathbf{u}(\mathbf{r}_i)) = 0$  leads to the characteristic speed  $|\mathbf{v}_i| \approx \sqrt{\alpha/\beta}$ . The fluid-free problem (Eq. 1 with  $\mathbf{u} = 0$ ) has been very well studied. Generally, particles are subject to two tendencies: changing their separations to minimize  $\Phi$  and adjusting their speeds to match the zeros of  $\mathbf{f}_M$ . Depending on initial conditions, dimensionality, number of particles and/or parameter choices, both constraints can be simultaneously satisfied, leading, for example, to rigidly translating flocks. If only one constraint is satisfied, mills, rigid disks, or random motion arise [18].

To distinguish between clear and opaque fluids, we introduce a ‘‘perception coefficient’’  $0 \leq \lambda \leq 1$  that measures the importance of the surrounding flow field in the speed-regulation process. For  $\lambda = 0$ , the fluid is ‘‘clear’’ and swimmers can ascertain their lab-frame velocities  $\mathbf{v}_i$ . In this case, fluid forces on particle  $i$  will simply take the form

$-\gamma(\mathbf{v}_i - \mathbf{u}(\mathbf{r}_i))$ , where both  $\mathbf{v}_i$  and  $\mathbf{u}(\mathbf{r}_i)$  are lab-frame velocities. For  $\lambda = 1$ , swimmers have no knowledge of the lab frame and can only adjust their motion in relation to the local fluid. In this case, the relative velocity  $\mathbf{v}_i - \mathbf{u}(\mathbf{r}_i)$  must be used in place of the lab-frame velocity  $\mathbf{v}_i$  in  $\mathbf{f}_M$  and Eq. 1. For  $0 \leq \lambda \leq 1$ , the particle model can be succinctly written as

$$m\dot{\mathbf{v}}_i = \left( \alpha - \beta |\mathbf{v}_i - \lambda \mathbf{u}(\mathbf{r}_i)|^2 \right) (\mathbf{v}_i - \lambda \mathbf{u}(\mathbf{r}_i)) - \gamma(\mathbf{v}_i - \mathbf{u}(\mathbf{r}_i)) - \nabla_i \sum_{j \neq i} \Phi(|\mathbf{r}_i - \mathbf{r}_j|). \quad (5)$$

Disturbances to the fluid are generated in two ways: self-propelled motion of individual swimmers imparting a flow  $\mathbf{u}_s(\mathbf{r})$ , and pairwise particle interactions imparting a fluid flow  $\mathbf{u}_p(\mathbf{r})$ . If the fluid is incompressible and at low Reynolds number, we can approximate the velocity field by the solution to Stokes' equation. Since the fluid dynamics are linear, the individual sources of the total fluid flow  $\mathbf{u}(\mathbf{r}) \equiv \mathbf{u}_s(\mathbf{r}) + \mathbf{u}_p(\mathbf{r})$  can be decoupled.

We do not treat the microscopic geometric details of how a particle propels itself except but rather employ a stroke-averaged model where period-averaged ‘‘strokes’’ are described as a force dipole acting on the fluid [62]. The self-propulsion force dipoles of a collection of swimmers generate the flow field

$$\mathbf{u}_s(\mathbf{r}) = \sum_j v_j \frac{G}{R_j^2} \left[ 3 \left( \hat{\mathbf{R}}_j \cdot \hat{\mathbf{v}}_j \right)^2 - 1 \right] \hat{\mathbf{R}}_j, \quad (6)$$

where  $\mathbf{R}_j \equiv (\mathbf{r} - \mathbf{r}_j)$ ,  $R_j \equiv |\mathbf{R}_j|$ ,  $\hat{\mathbf{R}}_j \equiv \mathbf{R}_j/R_j$ ,  $v_j \equiv |\mathbf{v}_j|$ , and  $\hat{\mathbf{v}}_j \equiv \mathbf{v}_j/v_j$ . The lumped parameter  $G$  depends on the detailed swimmer geometry such as the length of the swimmer and its longitudinal mass distribution and carries units of a length squared. For  $G > 0$ , the orientation of the force dipole is parallel to the swimmer's velocity, describing a propelling swimmer or a ‘‘pusher’’; conversely,  $G < 0$  denotes a contractile swimmer or a ‘‘puller’’. To model  $\mathbf{u}_p(\mathbf{r})$ , we neglect the finite size  $a$  of swimmers but include the particle interaction-mediated force density  $\mathbf{F}(\mathbf{r}) \approx -\sum_i \sum_{j \neq i} \delta(\mathbf{r} - \mathbf{r}_i) \nabla_i \Phi(\mathbf{r}_i - \mathbf{r}_j)$  in Stokes' equation:

$$\rho \frac{\partial \mathbf{u}_p}{\partial t} = \eta \nabla^2 \mathbf{u}_p - \nabla p + \mathbf{F}(\mathbf{r}), \quad (7)$$

where  $\rho$  and  $\eta$  are the density and the dynamic viscosity of the fluid, respectively and  $p$  is the local pressure field. Finally,  $\mathbf{F}(\mathbf{r}) \approx -\sum_i \sum_{j \neq i} \delta(\mathbf{r} - \mathbf{r}_i) \nabla_i \Phi(\mathbf{r}_i - \mathbf{r}_j)$  denotes the force density acting on the fluid, where  $\delta(\mathbf{x})$  is the Dirac delta-function. In the quasi-static limit in 3D,  $\mathbf{u}_p(\mathbf{r})$  can be calculated analytically as the steady-state solution to Eq. 7 using the incompressibility condition  $\nabla \cdot \mathbf{u}_p(\mathbf{r}) = 0$  and in terms of the static Oseen tensor

$$\mathbf{u}_p(\mathbf{r}) = -\sum_j \sum_{k \neq j} \frac{[\mathbf{I} + \hat{\mathbf{R}}_j \hat{\mathbf{R}}_j]}{8\pi\eta R_j} \cdot \nabla_j \Phi(|\mathbf{r}_j - \mathbf{r}_k|), \quad (8)$$

where  $\mathbf{I}$  is the identity matrix. Note that in contrast to the  $1/R^2$  dependence of  $\mathbf{u}_s$  in Eq. 6,  $\mathbf{u}_p$  can be longer ranged, decaying as  $1/R$ . While we neglect the inertia of the fluid by assuming zero Reynolds number (or  $\nu \equiv \eta/\rho \rightarrow \infty$ ) we retain particle inertia, implicitly assuming that particle mass density is much higher than fluid mass density.

In the remainder of this paper, we investigate swarming in zero Reynolds-number viscous fluids. Inertial flows given by the complete time-dependent solution of Eqs. 7 can be expressed in terms of a dynamic Oseen tensor as shown in the SI. In the extreme limit of  $\nu \rightarrow 0$ , either the fluid inertia is too large ( $\rho \rightarrow \infty$ ) to induce any flow field, or the fluid becomes inviscid ( $\eta \rightarrow 0$ ). For inviscid fluids the induced hydrodynamic interaction can be described as a potential flow and is dipolar, which is even shorter-ranged than the force-dipole-generated  $\mathbf{u}_s(\mathbf{r})$  considered in this paper. For completeness, we derive interaction-induced inviscid fluid flow in the Supporting Information (SI).

Henceforth, we non-dimensionalize space and time according to  $\mathbf{r}' = \frac{\sqrt{\alpha\beta}}{m}\mathbf{r}$  and  $t' = \frac{\alpha}{m}t$ . All other dimensionless model parameters are given in the SI. We also drop the prime superscripts and define the full fluid-coupled swarming model as  $\dot{\mathbf{r}}_i = \mathbf{v}_i(t)$  and

$$\begin{aligned} \dot{\mathbf{v}}_i = & \left(1 - |\mathbf{v}_i - \lambda\mathbf{u}(\mathbf{r}_i)|^2\right) (\mathbf{v}_i - \lambda\mathbf{u}(\mathbf{r}_i)) \\ & - \gamma(\mathbf{v}_i - \mathbf{u}(\mathbf{r}_i)) - \nabla_i \sum_{j \neq i} \Phi(|\mathbf{r}_i - \mathbf{r}_j|), \end{aligned} \quad (9)$$

where  $\mathbf{u}(\mathbf{r}) = \mathbf{u}_s(\mathbf{r}) + \chi\mathbf{u}_p(\mathbf{r})$  and  $\mathbf{u}_s(\mathbf{r})$  and  $\mathbf{u}_p(\mathbf{r})$  are given by Eqs. 6 and 8, respectively. We have introduced the toggle  $\chi = 0$  or 1 in the definition of  $\mathbf{u}(\mathbf{r})$  allows us to switch off the interaction-induced flow field  $\mathbf{u}_p$  (by setting  $\chi = 0$ ). To switch off the swimmer-induced flows only we set  $G = 0$  and take  $\chi = 1$ . The inclusion of both flows requires a non-zero  $G$  and  $\chi = 1$ .

**Implementation** – We numerically solve the quasistatic limit of Eq. 9 with  $\mathbf{u}_s(\mathbf{r})$  given by Eq. 6 and  $\mathbf{u}_p(\mathbf{r})$  by Eq. 8 using the fourth-order Runge-Kutta method with an adaptable time step size [76]. Since both  $\mathbf{u}_s(\mathbf{r})$ ,  $\mathbf{u}_p(\mathbf{r})$  depend on particle positions, they are updated at each time step. Initial conditions are defined by still particles placed at uniformly distributed random positions within a  $3\ell_a^3$  box which is removed after the start of the simulation. Unless otherwise specified, we set dimensionless Morse-potential parameters to  $C_a = 1.0$ ,  $\ell_a = 2.0$ ,  $C_r = 2.0$ ,  $\ell_r = 1.0$ , representing long-ranged attraction and short-ranged repulsion [7, 8, 18]. Modifications to potential parameters are discussed in the SI. Finally, to counter the collapsing tendency between particle pairs due to the  $1/R^2$  dependence of  $\mathbf{u}_s(\mathbf{r})$ , we add to  $\Phi(|\mathbf{r}_i - \mathbf{r}_j|)$  an extremely short-ranged diverging repulsive potential  $\sim 1/R^{12}$  to keep particles reasonably apart. We numerically investigate our model for different values of dynamic viscosity  $\eta$  and swimmer propulsion strength  $G$ .

## Results and Discussion

**Fluid-free limit** – For reference, we first consider  $\lambda = \gamma = 0$  where particle and fluid dynamics decouple. Eqs. 1 and 3 now reduce to the 3D version of the well-studied 2D swarming model presented in [16, 18]. While studies of 3D swarms have previously been examined [44], the full dynamics including the emergence of transient structures has not been explored. For the interaction parameters chosen above, possible coherent states in 2D include a flock, a single

rotating mill, and two counter-rotating mills [77]. In 3D we do not find counter-rotating mills: only simple mills and flocks can arise from random initial conditions, as shown in Fig. 1. The absence of counter-rotating mills in 3D can be easily understood. In 2D there are only two possible rotating directions, but in 3D there are an infinite number of rotational axes. Reversing rotating directions in 2D requires the angular momentum to change signs, but in 3D the rotational axes of a sub-mill can continuously evolve along the third dimension until all particles eventually come to rotate about a common axis. This picture is consistent with diffusion of angular momentum in 3D swarms [43].

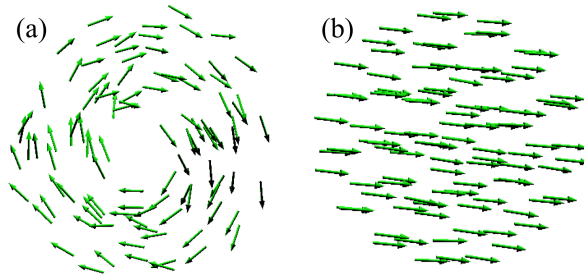


FIG. 1: Snapshots of typical 3D swarm patterns for 100 particles. (a) a rotational mill, and (b) a translating flock.

Most notably, despite being the dominant steady state in 2D, the single rotating mill shown in Fig. 1(a) is not a true 3D steady state. Although particles may settle into identifiable mills, extensive simulations performed on a variety of initial conditions show that a mill in 3D will eventually acquire a non-zero center-of-mass velocity and evolve into a flock as shown in Fig. 1(b). In Fig. 2(a), we plot the state indicator  $I_s$  defined in the SI to characterize the swarming pattern. A value of  $I_s = +1$  represents a perfect unidirectional flock,  $I_s = 0$  represents a random collection of particles, and  $I_s = -1$  indicates a perfect rotating mill. In particular, the red curve in Fig. 2(a) shows particles settling into a transient mill for a lengthy period of time before evolving into a translating flock; in contrast, the blue curve shows particles forming a flock without first assembling into a long-lived mill. In the latter case  $I_s$  can first decrease before rising back to  $I_s \approx 1$ .

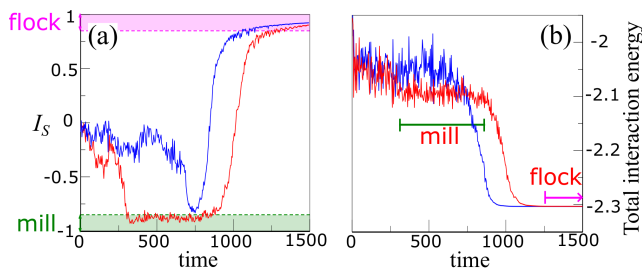


FIG. 2: (a) 3D simulations of Eqs. 1-4 without hydrodynamic interactions. The classifier of swarming patterns  $I_s$  is defined in the SI. The red curve denotes a swarm that first forms a mill before turning into a uniformly translating flock, while the blue curve shows particles evolving into a flock without first forming a mill. We empirically set thresholds  $I_s \leq -0.85$  (green) to signal mills and  $I_s \geq 0.85$  (magenta) to identify migrating flocks. We require a swarm to maintain the  $I_s$  value in either the two ranges for a period of 100 time units or more to be classified as a mill or flock. This criterion corresponds roughly to the time for a particle to circle a mill at least 10 times. (b) The total interaction energy  $\sum_{i,j} \Phi(|\mathbf{r}_i - \mathbf{r}_j|)/2$  corresponding to the two simulations above. The translating flock has a lower interaction energy than the mill.

To understand how mills and flocks develop in 3D, in Fig. 2(b) we plot the evolution of the total interaction energy  $\frac{1}{2} \sum_{i,j} \Phi(|\mathbf{r}_i - \mathbf{r}_j|)$  associated with the two simulations in Fig. 2(a), showing a lower total energy for the flock state.

Note that when assembled into flocks, particles settle into positions that correspond to the *global* minimum of the total potential energy. In contrast, when assembled into mills, only a *local* minimum of the total potential energy is attained. The net interaction force on each particle provides the centripetal force necessary to sustain the rotational movement. Although its energy is lower, for particles at random initial conditions, a flock may be kinetically less accessible than a mill. A mill is a state of local coherence, where particles match velocities with their close neighbors only, as opposed to a flock where global coherence arises from all particles moving in unison. As a result, 3D mills often emerge first out of a randomized configuration. For the same reason, 2D mills are not only stable at steady-state, but also dominate over flocks. However, 3D mills are unstable since they slowly acquire a translational momentum along the rotational axis aligned with the third direction. As particle velocities gradually become aligned with this translational momentum, the rotational unit turns into a spiral with continuously reduced angular speed, finally settling into an equilibrium lattice formation migrating at a uniform velocity. This effect cannot arise in 2D.

**Swimmer-induced fluid flow  $\mathbf{u}_s$**  – Next, we set  $\chi = 0$ , neglect the interaction-induced flow  $\mathbf{u}_p$ , and explore how  $\mathbf{u}_s$  affects swarm dynamics and how fluid-mediated patterns differ from those described in the fluid-free case above.

In general, the extensional flow generated in the reference frame of a puller ( $G < 0$ ) converge along the direction of motion and diverge along the perpendicular direction. Pusher-generated extensional flows move in an opposite direction, diverging along the direction of motion and converging laterally. As a result, pullers tend to flatten flocks into oblate shapes while pushers tend to form longitudinally-stretched prolate flocks. These deformed flocks are depicted in Fig. 3 for an opaque fluid.

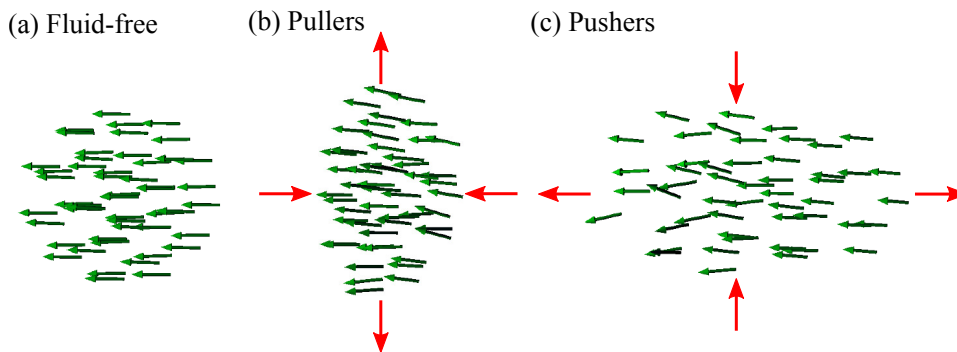


FIG. 3: Snapshots of 50-particle simulations showing three-dimensional flock formations arising in opaque fluids ( $\lambda = 1$ ) when  $\chi = 0$  ( $\mathbf{u}_p = 0$ ). (a) A stable spherical flock forms when self-generated flows are ignored ( $G = 0$ ). (b) A transient prolate flock forms when  $G = 0.15$  (pusher). (c) A transient oblate flock arises when  $G = -0.15$  (puller). The configuration shown in (a) was used as the initial condition for the simulations shown in (b) and (c). The red arrows indicate the direction of  $\mathbf{u}_s$  in the frame of the flock center-of-mass. In these simulations, the prolate flock is transitioning into a peloton, while the oblate flock is transitioning into a random blob. These deformed flocks are stable only if  $|G|$  is small, but with much less distortion.

In clear fluids ( $\lambda = 0$ ), the energy of a swarm dissipates significantly through the fluid drag term, slowing particle motion and reducing  $\mathbf{u}_s$ . For very large dimensionless drag  $\gamma \gg 1$ , both types of swimmers are arrested and  $\mathbf{u}_s \rightarrow 0$ . For intermediate  $\gamma$ , pushers align into prolate flocks and move at a reduced equilibrium speed of approximately  $\sqrt{1-\gamma}$ ; pullers also move at a reduced speed, but mostly at random without exhibiting any spatial order. The  $\gamma \rightarrow 0$  limit is the fluid-free case.

We observe a more diverse swarm morphologies in opaque fluids ( $\lambda = 1$ ) where the self propulsion term  $\mathbf{f}_M$  imparts sufficient energy to the particles to keep them moving at full unit speed relative to the background flow. In this

case, the oblate/prolate deformation of flocks is more pronounced than in clear fluids. In Fig. 4(a) we show the time evolution of 50 particles for  $|G| = 0.096$ . The red (blue) curves represent pullers (pushers). For reference we also plot the fluid-free case ( $G = 0$ ) in the green curve. For the small  $G = 0.096$ , pusher-generated flows suppress transient milling seen in the fluid-free case leading to a stable prolate flock. However, unlike the fluid-free case, pusher-generated flocks are not perfect and  $I_s \approx 0.75 < 1$ . Here, the spatial-temporal variations in  $\mathbf{u}_s$  impart fluctuations in the particles, preventing a perfectly aligned flock. Puller-generated flows, on the other hand, allow for the formation and permanence of mills: the mill-to-flock transition that occurs in the fluid-free case is blocked by the fluctuating flow field allowing mills to be long-lived. However, similar to pusher-generated flocks, puller-generated mills are constantly disturbed by  $\mathbf{u}_s$ . Particles in such mills occasionally deviate from their circulating trajectories, leading to a striking intermittent disintegration and re-assembling of the mills. In Fig. 4(b), we conduct a more thorough investigation of long-time swarming patterns by varying  $|G|$  for pullers (blue) and pushers (red). Pushers assemble into flocks as  $|G|$  increases, but patterns are increasingly disturbed by  $\mathbf{u}_s$ , leading to decreased  $I_s$ .

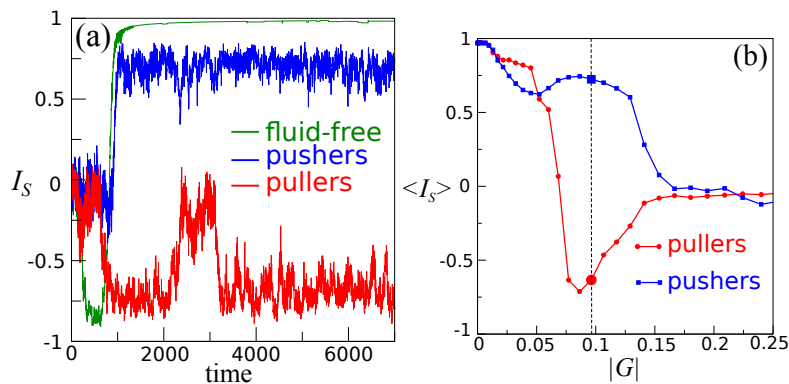


FIG. 4: (a) Time dependent swarm morphologies starting from random initial conditions. Pusher swarms ( $G = 0.096$ , blue curve), evolve directly towards a fluctuating flock, while puller swarms ( $G = -0.096$ , red curve) assemble into rotating mills; the latter persists indefinitely but is intermittently interrupted by bursts of randomness. For comparison, we also plot the fluid-free case ( $G = 0$ , green curve), where particles transiently form a mill before eventually assembling into a flock. (b) Long-time formations ( $t > 2000$ ) of pushers and pullers with different  $G$  values. The indicator  $\langle I_s \rangle$  is averaged for all time steps between  $2000 \leq t \leq 3000$  and over ten simulations. For pullers, persistent mills only occur approximately in the range of  $0.07 \leq G \leq 0.1$ ; below this range, flocks dominate, similarly to the fluid-free case; above this range, the swarm is in a permanent random state. Pushers always assemble into flocks; for large  $G$ , however, the flow field induces a peloton-like movement within the swarm, which pushes  $I_s$  towards zero.

For larger  $G$ ,  $\mathbf{u}_s$  induced by the pushers is strong enough to induce a novel “peloton”-like movement, where leading particles continuously recirculate toward the back end of the flock, as depicted in Fig. 5. When assembled into a peloton,  $I_s$  drops to nearly zero, although the majority of particles are still aligned. Pullers on the other hand tend to keep milling as  $|G|$  increases rather than transition to a flock. Here  $I_s \approx -1$ . For very large values of  $|G|$  the strong flow field prevents even mills from forming, and particle movement remains random. Overall, our results suggest that pusher-generated flow fields generally promote particle velocity ordering along a common direction but that an orthogonal component of the flow prevents perfect alignment for small  $G$  and ultimately to particles recirculating for large  $G$ . Puller-generated flow fields instead introduce more randomness preventing the mill to flock transition for small  $|G|$  and completely preventing a mill from forming for larger  $|G|$ .

**Interaction-induced fluid flow  $\mathbf{u}_p$**  – We now examine the effects of  $\mathbf{u}_p$  on swarm dynamics and analyze how

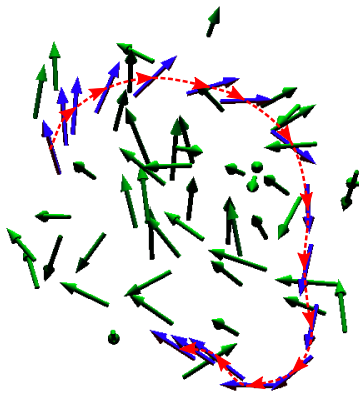


FIG. 5: A snapshot of a peloton-like formation for  $G = 0.15$ . The positions and velocities of the particles are represented by the green arrows, while the blue arrows tracks one particular particle for 15 steps prior to the snapshot. The red dashed line traces the trajectory of the blue particle which is initially near the leading edge of the flock, gets swept aside by the surrounding flow field, and then rejoins the flock near the back end.

patterns differ when compared to the fluid-free case. For a clear fluid ( $\lambda = 0$ ) our simulations reveal that at steady state particles either stop or assemble into a flock. The resulting speed can be evaluated by balancing self-propulsion with drag, yielding a dimensionless flock speed  $\sqrt{1-\gamma}$  for  $\gamma \leq 1$  and 0 for  $\gamma > 1$ , which are both confirmed by simulations. In physical units, the friction threshold for immobilizing a flock is  $6\pi\eta a > \alpha$ . Hydrodynamic coupling in a viscous clear fluid simply slows or stops translational flock motion. Note that in the  $a \rightarrow 0$  point-particle limit, drag is negligible and swarming in a clear fluid reduces to the canonical fluid-free problem.

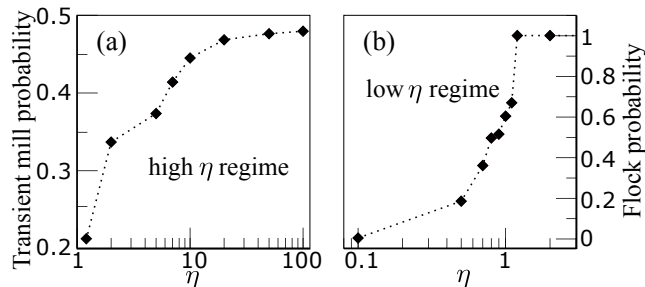


FIG. 6: Properties of swarms as  $\eta$  is varied in an opaque fluid. The plots show the probabilities of the simulations starting from random initial conditions that evolve into the indicated morphology. The curves are based on 100 realizations for each data point. (a)  $\eta \geq 1.2$ . Although in this high viscosity regime all initial conditions eventually settle into uniformly translating flocks, the probability of first forming a transient mill decreases with decreasing  $\eta$ . (b)  $\eta \leq 2$ . A uniformly translating flock is no longer the only final outcome when  $\eta < 1.2$ ; the probability of ending in such a state decreases with decreasing  $\eta$ .

As with swimmer-induced flows, the opaque fluid case is much more interesting. Here steady-state configurations depend nontrivially on the dimensionless viscosity  $\eta$  (defined in the SI) which measures ratio of the fluid momentum relaxation time to the time scale of the particle movement, thus representing an effective Deborah number for the problem [59, 78]. The parameter  $\eta$  appears in Eq. 9 through  $\mathbf{u}_p(\mathbf{r})$  in Eq. 8 and through  $\gamma = 6\pi\eta a$ . We assume small particles and neglect this latter drag interaction. As can be seen from Eq. 8,  $\mathbf{u}_p$  decreases with  $\eta$  so that as  $\eta$  increases the dynamics resembles that of the fluid-free case. Indeed, we find that for  $\eta > 1.2$ , flocks are the only stable steady-state solution for all random initial conditions used, similar to the fluid-free case. However, transient

mills can form before the permanent flock is assembled, with the probability of transient mills occurring decreasing with  $\eta$ . As shown in Fig. 6(a), for  $\eta = 100$  particles form mills before finally settling into flocks for about 50% of the random initial conditions used; this ratio drops to about 20% at  $\eta = 1.2$ . These qualitative findings in the  $G = 0$ ,  $\chi = 1$  regime are tabulated in Table 1.

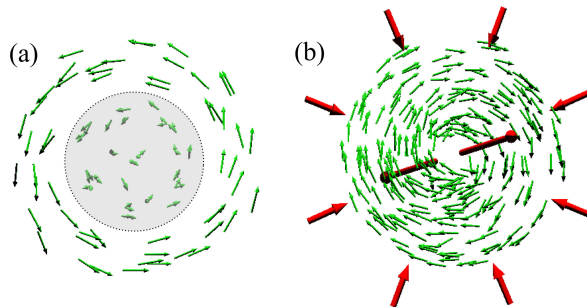


FIG. 7: (a) A mill-like formation induced by hydrodynamic interactions in the opaque fluid environment with  $\lambda = 1$  and  $\eta = 0.7$ . The gray shading delineates a disordered core that grows as  $\eta$  is decreased. (b) The induced flow field (red arrows) relative and the mill formation (green arrows, 250 particles). The fluid flow converges toward the central core along the plane of rotation. To balance the influx, a jet along the axis of rotation ejects the fluid from the central core.

$\eta$ \ time	intermediate $t$	long $t$
$\eta > 1.2$	mill or flock	flock only
$0.1 < \eta < 1.2$	mill or flock random	flock mill-like random
$\eta < 0.1$	random	random

TABLE I: Swarming structures observed in simulations for intermediate and long ( $t > 3000$ ) times under the  $\mathbf{u}_p$  flow field and as a function of the dimensionless fluid viscosity  $\eta$ . Steady state configurations take longer to assemble here than under  $\mathbf{u}_s$ . In the fluid-free case only flocks arise at long times. A moderately viscous fluid allows for the emergence of permanent mill-like structures and random aggregates.

Below  $\eta \approx 1.2$ , swarms experience a qualitative change in behavior and flocks are no longer the only long-lived steady-state. Fig. 6(b) shows that the probability of final flock formation decreases from unity at  $\eta \approx 1.2$  to zero at  $\eta \approx 0.1$ . In this intermediate range of  $\eta$ , two other long-lived configurations can arise: a mill-like formation as shown in Fig. 7(a), and a perpetual random swarm. Unlike the annular- or toroidal-shape of a classical mill, the hydrodynamically-mediated 3D mill-like structure has a central core filled with randomly moving particles. As the dimensionless viscosity decreases from  $\eta \approx 1.2$ , the randomly-moving core particles in a mill-like swarm expand their boundaries and eventually swallow the coherent part of the mill. The resulting pattern is one of perpetual random motion without any identifiable spatial order. Finally, for  $\eta \lesssim 0.1$ , swarms immediately collapse into the above described blob of perpetual random movement. All possible swarming patterns are listed in Table 1 as a function of the dimensionless viscosity  $\eta$ . A viscous flow  $\mathbf{u}_p$  in an opaque fluid thus allows for the emergence of persistent mill-like structures not observed in the absence of fluid flows.

We can also examine the induced flow fields in relation to particle velocities, and how they may drive transitions

among various swarm morphologies. Starting from a high- $\eta$  transient mill regime ( $\eta \gtrsim 1.2$ ), Fig. 7(b) qualitatively indicates the instantaneous direction of the hydrodynamic velocity field  $\mathbf{u}_p(\mathbf{r})$  (red arrows) induced by a mill-like formation of 250 particles. In a transient mill, the net particle-particle interactions provide the centripetal force that sustains rotation. This net force is imparted on the fluid, inducing an inward flow along the plane of rotation. The incompressible fluid is then ejected outward along the rotational axis, resembling a “jet” emanating from the center of an accretion disk. This outward jet entrains particles that wander into the core region, slowly disrupting the mill.

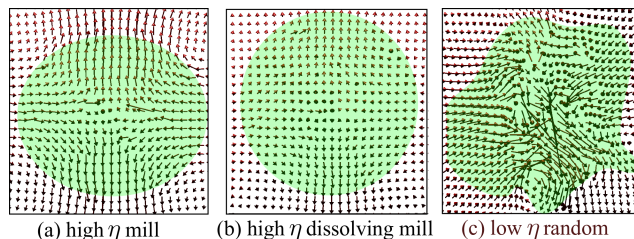


FIG. 8: Fluid velocity fields  $\mathbf{u}_p(\mathbf{r})$  associated with particle swarms (concentrated within the green shaded regions). (a) For large  $\eta$ , an early flow field resembles a jet. (b) At longer times with large  $\eta$ , the jet is eventually disrupted and a flock forms. (c) For very low  $\eta < 0.1$ , the disordered core region of a transient mill-like swarm will always expand leading to random particle velocities and the fluid velocity fields.

Entrainment arises through the self-propulsion term  $\mathbf{f}_M$  in opaque fluids, and if appreciable, through viscous drag. Moreover, the inward flow on the rotational plane effectively extends the interaction range among particles, driving the system into a minimum-energy flock state. As  $\eta$  is decreased, the induced Stokes accretion flow increases and drives more particles into the core of the mill. Particle motion then becomes randomized, disrupting the outward jet and ultimately *hindering* the mill-to-flock transition that would otherwise occur smoothly. Swarms can thus be trapped in the mill-like formation shown in Fig. 7(a) indefinitely as listed in Table 1. At even lower values of  $\eta$ , coherence is lost by an expanding disordered core region. The fluid flow fields observed under different regimes of  $\eta$  are plotted in Fig. 8.

**Combined effects of  $\mathbf{u}_s$  and  $\mathbf{u}_p$**  – In light of the above discussions, we now consider the effects of superimposing the two fields so that  $\mathbf{u}(\mathbf{r}) = \mathbf{u}_s(\mathbf{r}) + \mathbf{u}_p(\mathbf{r})$ . The magnitudes of  $\mathbf{u}_s$  and  $\mathbf{u}_p$  can be varied independently, and are controlled by  $G$  and  $\eta$ , respectively. Fig. 9 shows a qualitative phase diagram for long-term swarm morphologies discovered in our study. The swarm structures are labeled in  $(G, \eta)$ -space. For small values of  $\eta$ , where  $\mathbf{u}_p$  is dominant, swarms assemble into a random state. Inclusion of  $\mathbf{u}_s$  adds randomness to the swarming pattern. As  $\eta$  increases, the effects of  $\mathbf{u}_p$  diminish relative to those of  $\mathbf{u}_s$ . Pelotons emerge on the right side of the figure for pushers, while long-lasting mills are identified for pullers in an intermediate range of negative  $G$  values; the  $\mathbf{u}_p$ -related patterns retreat toward the  $G = 0$  axis. Mill-like patterns (downward cyan triangles) exist only when  $G = 0$ , suggesting that such patterns are easily disrupted or prevented by  $\mathbf{u}_s$ . Flocks reside in the upper-middle region of the diagram, which is shifted toward the right side because pushers promote velocity alignment. With increasing  $G$ , flocks turn into pelotons until pelotons are indistinguishable from random blobs. For very negative  $G$ , puller-generated  $\mathbf{u}_s$  dominates, and the random state is the only stable formation.

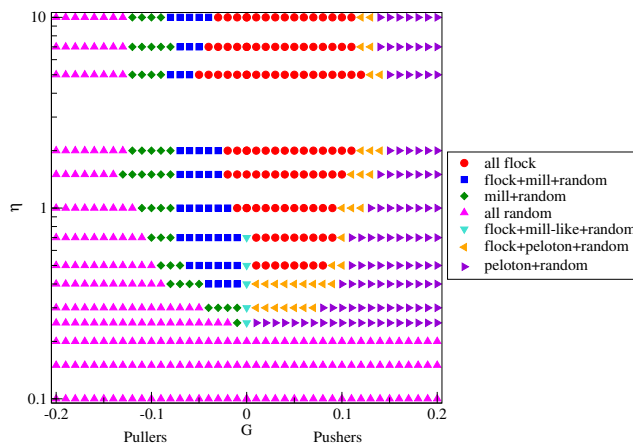


FIG. 9: A qualitative phase diagram delineating the possible persistent structures ( $t > 3000$ ) as a function of  $G$  and  $\eta$  in the presence of the total flow field  $\mathbf{u}(\mathbf{r}) = \mathbf{u}_s(\mathbf{r}) + \mathbf{u}_p(\mathbf{r})$ . Each point is based on 10 simulations. Flock formations are more likely to emerge for large  $\eta$ , and random states are more prominent for small  $\eta$ . For pullers ( $G < 0$ ), mills may appear with increasing  $|G|$ , but eventually random states dominate at large  $|G|$ . For weak pushers ( $G \gtrsim 0$ ), the flows promote flock formation; for large  $G$ , the flocks exhibit peloton-like movement. There is no clear distinction between flocks and pelotons; here we classify a recirculating flock as a peloton if  $I_s < 0.5$ .

### Summary and Conclusions

We derived a hydrodynamically coupled model for self-propelled swimmers in an incompressible zero-Reynolds-number Newtonian fluid. Under a force-free assumption, particle self-propulsion may generate a flow field that decays as  $1/r^2$ . We found that short-ranged conservative pairwise potentials can generate longer-ranged fluid motion decaying as  $1/r$  that can enhance particle interaction and greatly affect swarm morphology. In the absence of hydrodynamic coupling, 3D swarms exhibit much less diversity than in 2D, due to the additional dimension that provides a pathway for a variety of stable 2D patterns to transform into energy-minimizing, uniformly translating flocks in 3D.

In clear 3D fluid environments only flocks arise, similarly to the fluid-free scenario, albeit with particles moving at a reduced speed. In opaque 3D fluids, pusher generated flows accelerate particle alignment and suppress the emergence of metastable mills seen in the fluid-free case. Puller-generated flows, conversely, hinder particle velocity alignment, allowing transient mills to persist within certain viscosity ranges. Sufficiently strong puller flows disrupt any spatial order. Flows generated by particle-particle interactions kinetically accelerate the mill-to-flock transition. In high-viscosity opaque fluids, the hydrodynamic flow fields can form an accretion disk/jet structure associated with mills and entrain the self-propelled particles leading to quicker dissolution of the mill itself. However, at intermediate-viscosity opaque fluids, stronger hydrodynamic interactions may kinetically block the mill-to-flock transition, allowing a mill-like formation to form and persist. At even lower fluid viscosity  $\eta$ , swarms are completely chaotic. Since the Stokes equations used to describe the fluid flow are linear, the presence of both swimmer-induced and interaction-induced flow fields are also linearly additive. The final outcome depends on the relative strength between the two flows. Mill-like formations are absent. Although the drag coefficient  $\gamma = 6\pi\eta a > 0$ , we have assumed small particles and neglected viscous drag effects. For extremely large values of  $\eta$  drag may not be negligible even for small  $a$ . In this case, we expect particles to move at a lower speed but the qualitative sequence of patterns listed in Table 1 to remain valid.

Our results show that long-ranged nonconservative hydrodynamic forces can be induced by short-ranged conservative interactions, and, when combined with shorter-ranged self-propulsion-generated fluid flows, give rise to many new swarm morphologies and allow transitions between them. Our results suggest how hydrodynamics can conspire with intrinsic potential-derived interactions to kinetically control collective behavior in 3D swarms of self-propelled agents, particularly in opaque fluids.

### Acknowledgments

The authors thank Eric Lauga and Lae Un Kim for helpful discussions. This work was made possible by support from grants NSF DMS-1021818 (TC), NSF DMS-1021850 (MRD), ARO W1911NF-14-1-0472, and ARO MURI W1911NF-11-10332. MRD also acknowledges insights gained at the NAFKI conference on Collective Behavior: From Cells to Societies.

- 
- [1] H. Spohn, *Large Scale Dynamics of Interacting Particles*, Texts and Monographs in Physics (Springer, 1991).
  - [2] S. A. Kaufmann, *The origins of order: self-organization and selection in evolution* (Oxford Univ. Press, Oxford, 1993).
  - [3] T. Vicsek, A. Czirók, E. Ben-Jacob, I. Cohen, and O. Shochet, *Phys. Rev. Lett.* **75**, 1226 (1995).
  - [4] E. Albano, *Phys. Rev. Lett.* **77**, 2129 (1996).
  - [5] G. Flierl, D. Grünbaum, S. Levin, and D. Olson, *J. Theor. Biol.* **196**, 397 (1999).
  - [6] N. Shimoyama, K. Sugawara, T. Mizuguchi, Y. Hayakawa, and M. Sano, *Phys. Rev. Lett.* **76**, 3870 (1996).
  - [7] L. Edelstein-Keshet, J. Watmough, and D. Grünbaum, *J. Math. Biol.* **36**, 515 (1998).
  - [8] H. Levine, W. J. Rappel, and I. Cohen, *Phys. Rev. E* **63**, 017101 (2000).
  - [9] W. Ebeling and F. Schweitzer, *Theor. Biosci.* **120**, 207 (2001).
  - [10] J. Parrish, S. V. Viscido, and D. Grünbaum, *Biol. Bull.* **202**, 296 (2002).
  - [11] G. Grégoire, H. Chaté, and Y. Tu, *Physica D* **181**, 157 (2003).
  - [12] F. Chalub, P. A. Markowich, B. Perthame, and C. Schmeiser, *Monatsh. Math.* **142**, 123 (2004).
  - [13] I. D. Couzin, J. Krauss, N. R. Franks, and S. A. Levin, *Nature* **433**, 513 (2005).
  - [14] Y. Dolak and C. Schmeiser, *J. Math. Biol.* **51**, 595 (2005).
  - [15] D. Morale, V. Capasso, and K. Oelschläger, *J. Math. Biol.* **50**, 49 (2005).
  - [16] M. D'Orsogna, Y. Chuang, A. Bertozzi, and L. Chayes, *Phys. Rev. Lett.* **96**, 104302 (2006).
  - [17] F. Chalub, Y. Dolak-Struss, P. Markowich, D. Oelz, C. Schmeiser, and A. Soreff, *Math. Models and Methods in Appl. Sci.* **16**, 1173 (2006).
  - [18] Y. L. Chuang, M. R. D'Orsogna, D. Marthaler, A. L. Bertozzi, and L. Chayes, *Physica D* **232**, 33 (2007).
  - [19] A. Kaiser and H. Löwen, *Phys. Rev. E* **87**, 032712 (2013).
  - [20] S. K. You, *J. Korean Phys. Soc.* **63**, 1134 (2013).
  - [21] T. Schneirla, *Army Ants: A Study in Social Organization* (W.H. Freeman, 1971).
  - [22] S. Kim and D. Kaiser, *Science* **249**, 926 (1990).
  - [23] H. Niwa, *J. Theor. Biol.* **171**, 123 (1994).
  - [24] R. Dillon, L. Fauci, and D. G. III, *J. theor. Biol.* **177**, 325 (1995).
  - [25] W. Romey, *Ecol. Model.* **92**, 65 (1996).
  - [26] A. L. Koch and D. White, *Bioessays* **20**, 1030 (1998).

- [27] J. K. Parrish and L. Edelstein-Keshet, *Science* **284**, 99 (1999).
- [28] S. Camazine, J.-L. Deneubourg, N. R. Franks, J. Sneyd, G. Theraulaz, and E. Bonabeau, *Self-Organization in Biological Systems* (Princeton University Press, 2003).
- [29] A. Ordemann, G. Balazsi, and F. Moss, *Nova Acta Leopoldina* **88**, 87 (2003).
- [30] A. Oien, *Bull. Math. Biol.* **66**, 1 (2004).
- [31] P. Gómez-Moureló, *Ecol. Model.* **188**, 93 (2005).
- [32] R. Mach and F. Schweitzer, *Bull. Math. Biol.* **69**, 539 (2006).
- [33] A. M. Hein and S. A. McKinley, *PLoS Comput. Biol.* **9**, 31003178 (2013).
- [34] K. Sugawara and M. Sano, *Physica D* **100**, 343 (1997).
- [35] E. Bonabeau, M. Dorigo, and G. Theraulaz, *Swarm intelligence: from natural to artificial systems* (Oxford Univ. Press, Oxford, 1999).
- [36] N. E. Leonard and E. Fiorelli, *Proc. 40<sup>th</sup> IEEE Conf. Decision and Control* pp. 2968–2973 (2001).
- [37] V. Gazi and K. Passino, *IEEE T. Automat. Contr.* **48**, 692 (2003).
- [38] D. E. Chang, S. C. Shadden, J. E. Marsden, and R. Olfati-Saber, *Proc. 42<sup>nd</sup> IEEE Conf. Decision and Control* pp. 539–543 (2003).
- [39] A. Jadbabaie, J. Lin, and A. Morse, *IEEE T. Automat. Contr.* **48**, 988 (2003).
- [40] Y. Liu, K. M. Passino, and M. M. Polycarpou, *IEEE T. Automat. Contr.* **48**, 76 (2003).
- [41] Y. L. Chuang, Y. R. Huang, M. R. D’Orsogna, and A. L. Bertozzi, *IEEE International Conference on Robotics and Automation* pp. 2292–2299 (2007).
- [42] I. D. Couzin, J. Krause, R. James, G. D. Ruxton, and N. R. Franks, *J. Theor. Biol.* **218**, 1 (2002).
- [43] J. Strefler, U. Erdmann, and L. Schimansky-Geier, *Phys. Rev. E* **78**, 031927 (2008).
- [44] N. H. P. Nguyen, E. Jankowski, and S. C. Glotzer, *Phys. Rev. E* **86**, 011136 (2012).
- [45] G. Taylor, *Proc. R. Soc. Lond. A* (1951).
- [46] G. J. Hancock, *Proc. R. Soc. Lond. A* **217**, 96 (1953).
- [47] J. Blake, *J. Biomechanics* **6**, 133 (1973).
- [48] A. Shapere and F. Wilczek, *J. Fluid Mech.* **198**, 557 (1989).
- [49] G. P. Galdi, *Arch. Rational Mech. Anal.* **148**, 53 (1999).
- [50] L. E. Becker, S. A. Koehler, and H. A. Stone, *J. Fluid Mech.* **490**, 15 (2003).
- [51] A. Baskaran and M. C. Marchetti, *Phys. Rev. E* **77**, 011920 (2008).
- [52] S. E. Spagnolie and E. Lauga, *J. Fluid Mech.* **700**, 105 (2012).
- [53] E. Lauga and T. Powers, *Rep. Prog. Phys.* **72**, 096601 (2009).
- [54] S. M. Ross and S. Corrsin, *J. Appl. Physiol.* **37**, 333 (1974).
- [55] T. K. Chaudhury, *J. Fluid Mech.* **95**, 189 (1979).
- [56] G. R. Fulford, D. F. Katz, and R. L. Powell, *Biorheology* **35**, 295 (1998).
- [57] E. Lauga, *Phys. Fluids* **19**, 083104 (2007).
- [58] T. Normand and E. Lauga, *Phys. Rev. E* **78**, 061907 (2008).
- [59] E. Lauga, *Europhys. Lett.* **86**, 64001 (2009).
- [60] H. C. Fu, C. W. Wolgemuth, and T. R. Powers, *Phys. Fluids* **21**, 033102 (2009).
- [61] L. Zhu, E. Lauga, and L. Brandt, *Phys. Fluids* **24**, 051902 (2012).
- [62] A. Baskaran and M. C. Marchetti, *Proc. Natl. Acad. Sci. USA* **106**, 15567 (2009).
- [63] F. Cucker and S. Smale, *Japan. J. Math.* **2**, 197 (2007).
- [64] F. Cucker and S. Smale, *IEEE T. Automat. Contr.* **52**, 852 (2007).
- [65] J. Shen, *SIAM J. Appl. Math* **68**, 694 (2008).

- [66] S. Naseri and N. Phan-Thien, *Computational Mechanics* **20**, 551 (1997).
- [67] R. Cortez, N. Cowen, R. Dillon, and L. Fauci, *Comp. Sci. and Eng.* **6**, 38 (2004).
- [68] R. Cortez, L. Fauci, and A. Medovikov, *Phys. Fluids* **17**, 031504 (2005).
- [69] I. Riedel, K. Kruse, and J. Howard, *Science* **309**, 300 (2005).
- [70] C. W. Oseen, *Neuere Methoden und Ergebnisse in der Hydrodynamik* (Leipzig: Akademische Verlagsgesellschaft m.b.h., 1927).
- [71] O. A. Ladyzhenskaya and R. A. Silverman, *The mathematical theory of viscous incompressible flow* (Gordon and Breach Science Publishers, 1963).
- [72] R. Finn, *Arch. Rational Mech. Anal.* **19**, 363 (1965).
- [73] J. R. Blake, *Proc. Camb. Phil. Soc.* **70**, 303 (1971).
- [74] P. Español, M. Rubio, and I. Zúñiga, *Phys. Rev. E* **51**, 803 (1995).
- [75] J.-J. Shu and A. T. Chwang, *Phys. Rev. E* **63**, 051201 (2001).
- [76] G. H. Golub and J. M. Ortega, *Scientific Computing and Differential Equations: An Introduction to Numerical Methods* (Academic Press, 1987).
- [77] J. Carrillo, M. R. D'Orsogna, and V. Panferov, *Kin. Rel. Mod.* **2**, 363 (2009).
- [78] M. Reiner, *Physics Today* **17**, 62 (1964).
- [79] J. H. Irving and J. G. Kirkwood, *J. Chem. Phys.* **6**, 817 (1950).
- [80] F. Golse, *Journées équations aux dérivés partielles* **9**, 1 (2003).
- [81] J. R. Blake, *J. Austral. Math. Soc. Ser. B* **30**, 127 (1988).

## I. SUPPLEMENTARY INFORMATION

### II. CONTINUUM TWO-FLUID LIMIT AND STABILITY

We use the ‘‘Irving-Kirkwood’’ averaging approach [18, 79, 80] to derive a two-fluid continuum limit of our hydrodynamically-interacting opaque-fluid swarming model. To avoid the complexity of the microscopic geometry of swimmers, we restrict our analysis on case of  $G = 0$  and  $\chi = 1$ , leaving  $\mathbf{u}_p$  as the only fluid velocity. The results are continuum hydrodynamic equations for the *density*  $n(\mathbf{r})$  of self-propelled particles coupled to the Stokes equation obeyed by the opaque fluid medium:

$$\frac{\partial n}{\partial t} + \nabla \cdot (n\mathbf{v}) = 0, \quad (10)$$

$$\frac{\partial (n\mathbf{v})}{\partial t} + \nabla \cdot (n\mathbf{v}\mathbf{v}) = f(|\mathbf{v} - \mathbf{u}_p|) (\mathbf{v} - \mathbf{u}_p) - \mathbf{F}, \quad (11)$$

$$\rho \frac{\partial \mathbf{u}_p}{\partial t} = \eta \nabla^2 \mathbf{u}_p - \nabla p - \mathbf{F}, \quad (12)$$

$$\nabla \cdot \mathbf{u}_p = 0, \quad (13)$$

where  $\mathbf{v}$  is the locally averaged velocity field of the self-propelled particles,  $\mathbf{u}_p$  is the velocity field of the fluid medium, and  $f(v) \equiv \alpha - \beta v^2$  defines the self-propulsion of the particles. The interaction force coupling the two fluids is

$$\mathbf{F} = n(\mathbf{r}) \nabla_{\mathbf{r}} \int_{\mathbb{R}^3} \Phi(|\mathbf{r} - \mathbf{y}|) n(\mathbf{y}) d^3\mathbf{y}. \quad (14)$$

If a quasistatic fluid medium is assumed, along with vanishing  $\mathbf{u}_p$  and  $p$  at  $|\mathbf{r}| \rightarrow \infty$ , we find a homogeneous solution to the full model defined by

$$n(\mathbf{r}) = n_0, \quad \mathbf{v}(\mathbf{r}) = v_0 \hat{\mathbf{v}}, \quad \mathbf{u}_p = 0, \quad \text{and} \quad p = 0. \quad (15)$$

Here,  $v_0 \equiv \sqrt{\alpha/\beta}$ ,  $n_0$  is an arbitrary constant density, and  $\hat{\mathbf{v}}$  is an arbitrary orientation.

To examine the linear stability of this solution, we set  $\hat{\mathbf{z}} \parallel \hat{\mathbf{v}}$  and perturb the homogeneous solution according to

$$\begin{pmatrix} n \\ v_x \\ v_y \\ v_z \\ u_{p,x} \\ u_{p,y} \\ u_{p,z} \\ p \end{pmatrix} = \begin{pmatrix} n_0 \\ 0 \\ 0 \\ v_0 \\ 0 \\ 0 \\ 0 \\ 0 \end{pmatrix} + \begin{pmatrix} \delta n \\ \delta v_x \\ \delta v_y \\ \delta v_z \\ \delta u_x \\ \delta u_y \\ \delta u_z \\ \delta p \end{pmatrix} e^{-\sigma t + i\mathbf{q}\cdot\mathbf{x}}. \quad (16)$$

The dispersion relation that defines the relation between the growth rate  $\sigma$  and the wave vector  $\mathbf{q}$  is

$$\sigma^3 - v_0 f'(v_0) \sigma^2 + q^2 n_0 \tilde{\Phi} \sigma - (q_x^2 + q_y^2) n_0 v_0 f'(v_0) \tilde{\Phi} = 0, \quad (17)$$

where  $\tilde{\Phi}(|\mathbf{q}|)$  is the Fourier transform of the interaction potential. Since variations in  $\mathbf{u}$  affect the self-propelled particle momentum conservation only at quadratic order, it is not surprising that the linear stability condition ends up the same as the case without hydrodynamics. This result is identical to that arising in the no-fluid case of swarming in vacuum and already analyzed in detail [18]. Also note that the effects of  $\mathbf{u}_s$  have previously been analyzed with an inertia-less model of non-interacting swimmers and found to induce density instability for pullers and long-ranged correlation of orientations for pushers [62].

### III. NON-DIMENSIONALIZATION

The non-dimensional parameters used in Eq. 9 are defined as

$$\begin{aligned}
\mathbf{r}' &= \frac{\sqrt{\alpha\beta}}{m} \mathbf{r}, & t' &= \frac{\alpha}{m} t, \\
\mathbf{v}'_i &= \sqrt{\frac{\beta}{\alpha}} \mathbf{v}_i, & \mathbf{u}' &= \sqrt{\frac{\beta}{\alpha}} \mathbf{u}, & \gamma' &= \frac{\gamma}{\alpha}, \\
\rho' &= \frac{m^2}{\sqrt{\alpha^3\beta^3}} \rho, & \eta' &= \frac{m}{\sqrt{\alpha^3\beta}} \eta, & G' &= \frac{\alpha\beta}{m^2} G, \\
\Phi' &= \frac{\beta}{\alpha m} \Phi, & p' &= \frac{m^2}{\sqrt{\alpha^5\beta}} p, \\
C'_a &= \frac{\beta}{\alpha m} C_a, & C'_r &= \frac{\beta}{\alpha m} C_r, \\
\ell'_a &= \frac{\sqrt{\alpha\beta}}{m} \ell_a, & \ell'_r &= \frac{\sqrt{\alpha\beta}}{m} \ell_r.
\end{aligned} \tag{18}$$

#### IV. TIME-DEPENDENT STOKES FLOW

In the paper, we assume  $\nu \rightarrow 0$  for the (dimensionless) Stokes equation 9 and conduct our investigation at the quasistatic limit. More generally, the time-dependent velocity field can be expressed as

$$\mathbf{u}(\mathbf{r}_j, t) = \frac{1}{\rho} \sum_{i \neq j} \int_0^t dt' \mathbf{T}(\mathbf{r}_i - \mathbf{r}_j; t - t') \cdot \mathbf{f}_i, \tag{19}$$

where  $\rho$  is the mass density of the embedding Newtonian fluid and  $\mathbf{T}$  is the three-dimensional dynamic Oseen tensor given by [74]

$$\begin{aligned}
\mathbf{T}(\mathbf{r}, t) &= \int \frac{d^3\mathbf{k}}{(2\pi)^3} e^{-\nu k^2 t + i\mathbf{k} \cdot \mathbf{r}} [\mathbf{I} - \hat{\mathbf{k}}\hat{\mathbf{k}}] \\
&= p(r, t)\mathbf{I} - q(r, t)\hat{\mathbf{r}}\hat{\mathbf{r}},
\end{aligned} \tag{20}$$

with

$$\begin{aligned}
p(r, t) &= \left(1 + \frac{2\nu t}{r^2}\right) f(r, t) - \frac{g(r, t)}{r^2} \\
q(r, t) &= \left(1 + \frac{6\nu t}{r^2}\right) f(r, t) - \frac{3g(r, t)}{r^2} \\
f(r, t) &= \frac{1}{(4\pi\nu t)^{3/2}} \exp\left[-\frac{r^2}{4\nu t}\right] \\
g(r, t) &= \frac{1}{4\pi r} \operatorname{erf}\left(\frac{r}{\sqrt{4\nu t}}\right).
\end{aligned} \tag{21}$$

In the quasistatic limit, the Oseen tensor is

$$\frac{1}{\rho} \mathbf{T}(\mathbf{r}, t) \approx \frac{1}{8\pi\eta r} [\mathbf{I} + \hat{\mathbf{r}}\hat{\mathbf{r}}] \delta(t), \tag{22}$$

which is used in Eq. 8 to provide an analytic form of the velocity field. The solution to the pressure field  $p(\mathbf{r}, t)$  is also given; however, its effect on swimmers is ignored since its gradient is negligible across the size  $a \rightarrow 0$  of small particles.

## V. POTENTIAL FLOW

As derived in [81], the fluid velocity potential  $\phi(\mathbf{r})$  at a location  $\mathbf{r}$  from an accelerating spherical particle of radius  $a$  can be approximated in the far-field  $|\mathbf{r}| \gg a$  limit by the formula

$$\phi(\mathbf{r}, t) \sim -\frac{m(t)}{4\pi|\mathbf{r}|} - \frac{\mathbf{d}(t) \cdot \mathbf{r}}{4\pi|\mathbf{r}|^3} + \mathcal{O}\left(|\mathbf{r}|^{-3}\right), \tag{23}$$

where

$$m(t) = \oint_{\partial V} \nabla\phi \cdot d\mathbf{S}, \tag{24}$$

and

$$\mathbf{d}(t) = \oint_{\partial V} \phi d\mathbf{S} + \oint_{\partial V} \mathbf{r} \nabla\phi \cdot d\mathbf{S} \tag{25}$$

are obtained by integrating over the boundary  $\partial V$  of the spherical volume  $V$  of the source object. The near-field  $\phi$  in the integrands depends on the shape and swimming mechanism of the source object. Let us consider the simplest case of solid spherical particles moving through an inviscid fluid. For a lone particle of radius  $a$  traveling at a velocity

$\mathbf{v}$  as illustrated in Fig. 10, we may derive the fluid velocity potential in the laboratory frame as follows

$$\phi(\mathbf{r}) = -v \frac{a^3}{2|\mathbf{r}|^2} \cos \theta, \quad (26)$$

where  $v = |\mathbf{v}|$ ,  $\mathbf{r}$  is the a spatial position relative to the center of the particle, and  $\theta$  is the angle between  $\mathbf{r}$  and  $\mathbf{v}$ . Substituting Eq. 26 into Eqs. 24 and 25, we obtain

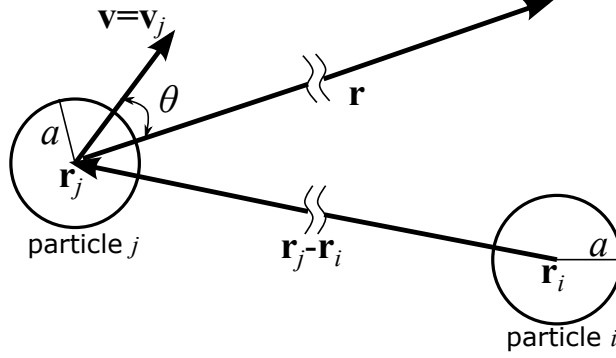


FIG. 10: Hydrodynamic interactions due to potential flow. Eqs. 23-28 calculate the approximated fluid potential at an arbitrary far-field location caused by acceleration by the particle  $j$ . Eqs. 30-33 derive the force induced by the fluid potential on particle  $i$ .

$$m(t) = 0, \quad \text{and} \quad \mathbf{d}(t) = 2\pi a^3 \mathbf{v}(t). \quad (27)$$

As a result, the far-field fluid velocity potential of the moving sphere is

$$\phi(\mathbf{r}, t) \sim -\frac{a^3 \mathbf{v}(t) \cdot \mathbf{r}}{2|\mathbf{r}|^3}, \quad (28)$$

Next, let us calculate the force induced by a moving particle at position  $\mathbf{r}_j$  on an identical particle at a position  $\mathbf{r}_i$ . We assume that  $|\mathbf{r}_i - \mathbf{r}_j| \gg a$ , so that the far-field approximation is appropriate. From the Euler equation of inviscid flow, we know that the fluid velocity potential  $\phi$  induces a pressure

$$p = p_0 - \rho \frac{\partial \phi}{\partial t} - \frac{1}{2} \rho |\mathbf{u}|^2, \quad (29)$$

where  $\rho$  is the fluid density,  $\mathbf{u} = \nabla \phi$  is the fluid velocity, and  $p_0$  is an arbitrary reference point of the pressure. The resultant force on a spherical object is found from integrating the pressure variation over its surface:

$$\begin{aligned}
\mathbf{F}_{\text{p.f.}} &= \oint_{\partial V} p d\mathbf{S} \\
&= - \oint_{\partial V} \rho \frac{\partial \phi}{\partial t} d\mathbf{S} \\
&= \frac{\rho}{4\pi} \frac{d\mathbf{d}(t)}{dt} \cdot \oint_{\partial V} \frac{(\mathbf{r} - \mathbf{s})}{|\mathbf{r} - \mathbf{s}|^3} \hat{\mathbf{s}} dS.
\end{aligned} \tag{30}$$

Here,  $\mathbf{r} \equiv \mathbf{r}_j - \mathbf{r}_i$ ,  $\mathbf{s}$  is a vector from the particle center to the particle surface, and  $\hat{\mathbf{s}} \equiv \mathbf{s}/|\mathbf{s}|$ . For a spherical particle of radius  $a = |\mathbf{s}| \ll |\mathbf{r}|$ , we use the approximation  $|\mathbf{r} - \mathbf{s}|^{-3} \simeq |\mathbf{r}|^{-3} \left(1 + 3(\mathbf{s} \cdot \mathbf{r})/|\mathbf{r}|^2\right)$  to find

$$\mathbf{F}_{\text{p.f.}} = \frac{\rho a^3}{3 |\mathbf{r}|^3} \dot{\mathbf{d}}(t) \cdot \left[ 3 \frac{\mathbf{r}\mathbf{r}}{|\mathbf{r}|^2} - \mathbf{I} \right]. \tag{31}$$

Substituting Eq. 25 into the above equation, we obtain

$$\mathbf{F}_{\text{p.f.}} = \frac{2\pi\rho a^6}{3 |\mathbf{r}|^3} \dot{\mathbf{v}}(t) \cdot \left[ 3 \frac{\mathbf{r}\mathbf{r}}{|\mathbf{r}|^2} - \mathbf{I} \right]. \tag{32}$$

Assuming there are  $N$  identical particles, the potential flow induced force on particle  $i$  is thus

$$\mathbf{F}_{\text{p.f.}}^i = \frac{2\pi\rho a^6}{3} \sum_{j \neq i}^N \frac{\dot{\mathbf{v}}_j(t)}{|\mathbf{r}_j - \mathbf{r}_i|^3} \cdot \left[ 3 \frac{(\mathbf{r}_j - \mathbf{r}_i)(\mathbf{r}_j - \mathbf{r}_i)}{|\mathbf{r}_j - \mathbf{r}_i|^2} - \mathbf{I} \right]. \tag{33}$$

Note that the force is short-ranged, of the order  $\mathcal{O}(|\mathbf{r}_j - \mathbf{r}_i|^{-3})$ . Moreover, its amplitude is proportional to  $a^6$ . As a result, the hydrodynamic interaction force induced by potential flows does not have significant impact on collective behavior particularly when  $\rho$  and/or the volume fraction of particles is small. If  $\rho$  is very large, the flow field imposes a repulsion between particles that encounter each other, potentially preventing them from forming a coherent structure.

## VI. INDICATOR OF THE SWARMING STATES

Here we define a metric to describe the state of a swarm. This quantity will consistently distinguish between parallel flock, single rotating mill, and random swarms. To identify the parallel flock state, we note that all particles are moving at the same velocity as the Center-of-Mass (CM) velocity. To find the rotating mill state, we take advantage of the fact that all particles share the same axis of rotation. We combine these properties into a single quantity  $I_s$  over the desired range  $[-1, 1]$  where  $-1$  is associated with a perfect mill and  $+1$  indicates a uniformly translating flock. The indicator  $I_s$  is decomposed according to

$$I_s \equiv I_{\text{flock}} - I_{\text{mill}}. \quad (34)$$

Given  $N$  particles,

$$I_{\text{flock}} \equiv 1 - \frac{\sum_i |\mathbf{v}_i - \mathbf{v}_{\text{CM}}|}{N\sqrt{\alpha/\beta}}. \quad (35)$$

Note that  $I_{\text{flock}} = 1$  for a perfect parallel flock and  $I_{\text{flock}} = 0$  for a perfect mill. To define  $I_{\text{mill}}$  we first compute the rotational axis  $\hat{\omega}_i$  of particle  $i$ :

$$\hat{\omega}_i(t) = \frac{\mathbf{v}_i(t) \times \mathbf{F}_i(t)}{|\mathbf{v}_i(t)| |\mathbf{F}_i(t)|}. \quad (36)$$

where  $\mathbf{F}_i$  is the force acting on particle  $i$ . We then evaluate the degree of alignment between all  $\hat{\omega}_i$  and define

$$I_{\text{mill}} = \frac{\sum_i \sum_{j \neq i} \hat{\omega}_i \cdot \hat{\omega}_j}{N(N-1)}. \quad (37)$$

Note that  $I_{\text{mill}} = 1$  when the rotations of all the particles are perfectly aligned and  $I_{\text{mill}} = 0$  when all particles are in a perfect parallel flock formation. Putting  $I_{\text{flock}}$  and  $I_{\text{mill}}$  together in  $I_s$  (Eq. 34), we find  $I_s = -1$  for a perfect mill and  $I_s = +1$  for a perfect flock. Finally, since swarms are seldom in a perfect formation, we considered thresholds on  $I_s$  as indicated in Fig. 2.

## VII. EFFECTS OF CHANGING INTERACTION POTENTIALS

All of the above results were obtained using a fixed set of potential parameters  $C_{r,a}, \ell_{r,a}$ . The primary effect of varying these parameters is to change the spatial size of swarms. For rotational mills, an increase in diameter is accompanied by a decrease in the magnitude of the centripetal force and weaker destabilizing flows. A larger swarm is also less sensitive to hydrodynamic effects since particles are spaced further apart, generating weaker interaction forces and hence weaker flows. In Fig. 11(a), we explore different potentials and test the robustness of flock formation in the low  $\eta$  regime where the flock can be broken up by hydrodynamic interactions. Not surprisingly, for potentials that are more ‘‘H-stable’’ [16, 18], the probability of stable flock formation increases. While H-stability is an equilibrium property that is insensitive to hydrodynamics [16, 18], our results suggest that H-stable flocks are more resistant to hydrodynamic disruption.

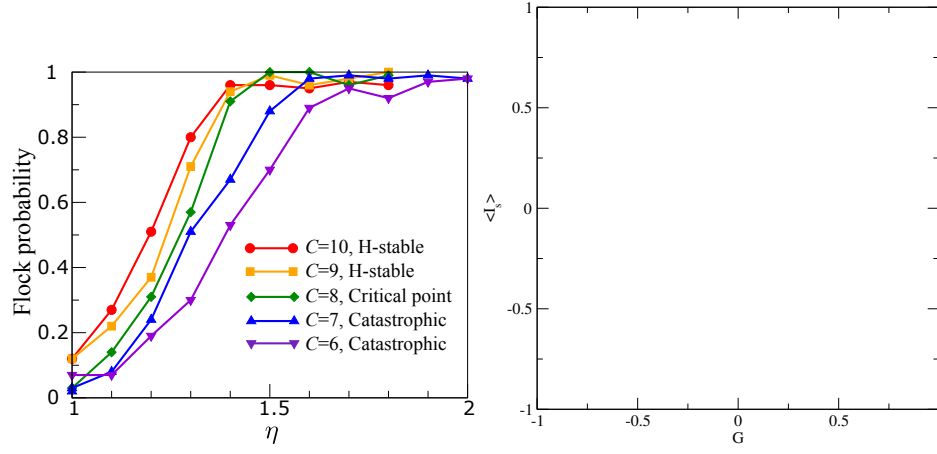


FIG. 11: The dependence of stable flock formation probability on potential types and opaque medium viscosity. Here, we fix  $\ell_a = 1$ ,  $\ell_r = 0.5$  and vary  $C \equiv C_r/C_a = 6 - 10$  while keeping  $C_a = 100$ . H-stable flocks are more robust against hydrodynamic disruption.